Available online at www.sciencedirect.com
SCIENCE DIRECT®
Ultrasonics 41 (2004) 743–753
Ultrasonics
www.elsevier.com/locate/ultras

The combined effect of nonlinear filtration and window size on the accuracy of tissue displacement estimation using detected echo signals

Vera Behar [a,*], Dan Adam [a], Peter Lysyansky [b], Zvi Friedman [b]

[a] Department of Biomedical Engineering, Technion-Israel Institute of Technology, Technion City, Haifa 32000, Israel
[b] GE Ultrasound Israel Ltd, Einstein Building, 7 Etgar Street, Tirat Hacarmel 39120, Israel

Received 6 September 2003; received in revised form 20 September 2003; accepted 22 September 2003

Abstract

In cardiac elastography, the regional strain and strain rate imaging is based on displacement estimation of tissue sections within the heart muscle carried out with various block-matching techniques (cross-correlation, sum of absolute differences, sum of squared differences, etc.). The accuracy of these techniques depends on a combination of ultrasonic imaging parameters such as ultrasonic frequency of interrogation, signal-to-noise ratio, size of a kernel used in a block-matching algorithm, type of data and speckle decorrelation. In this paper, we discuss the possibility to enhance the accuracy of the displacement estimation via nonlinear filtering of B-mode images before block-matching operation. The combined effect of a filter algorithm and a kernel size on the accuracy of the displacement estimation is analyzed using a 36-frame sequence of grayscale B-mode images of a human heart acquired by an ultrasound system operating at 1.77 MHz. It is shown that the nonlinear filtering of images enables to obtain the desired accuracy (less than one pixel) of the displacement estimation with smaller kernels than without filtering. These results are obtained for two filters—an adaptive anisotropic diffusion filter and a nonlinear Gaussian filter chain.

Keywords: Cardiac elastography; Motion estimation; Nonlinear image filtration; Statistical estimation

1. Introduction

Elastography is a technique for imaging the elastic properties of tissue that produces ultrasound images called elastograms, using displacements of tissue elements caused by tissue contractions. The method, proposed by Ophir et al., estimates local tissue strain resulting from an external compression applied to the tissue [1]. In cardiac echocardiography, as the heart undergoes periodic deformations during the contraction and the relaxation phases, the estimation of these deformations is termed cardiac elastography and is used for detection and mapping of cardiac ischemia or infarction [2,3]. In cardiac elastography, displacement and strain estimates are obtained from multiple sonographic views of a heart, utilizing RF data [2], or envelope-detected data [3]. Various 2D-tracking techniques have been proposed for ultrasonic displacement estimation. These techniques determine the local displacement vectors of speckle patterns in sequential images, usually using a block-matching algorithm. A block-matching algorithm usually maximizes the normalized cross-correlation function (NC) between the matching blocks in the "reference" and "test" images, so that the probability that a displacement estimate represents the "true" tissue displacement in an image, is also maximized [4]. Since the computational load of estimating the cross-correlation is very high, in practice two essentially equivalent approaches are often used, the sum of absolute differences (SAD) and the sum of squared differences (SSD) [5,6]. The accuracy of the displacement estimation depends on a set of the ultrasound imaging system parameters—the frequency of interrogation, the signal-to-noise ratio (SNR), the size of the kernel used in the block-matching algorithm, the type of data (RF or

* Corresponding author.
E-mail addresses: vera@bm.technion.ac.il (V. Behar), dan@bm.technion.ac.il (D. Adam), peter.lysyansky@med.ge.com (P. Lysyansky), zvi.friedman@med.ge.com (Z. Friedman).

0041-624X/$ - see front matter © 2003 Elsevier B.V. All rights reserved.
doi:10.1016/j.ultras.2003.09.003

envelope) and speckle decorrelation [7–12]. Results recently published show that for a high SNR, a high signal correlation, and a large kernel size, the accuracy of block-matching algorithms (NC, SAD or SSD) is close to the theoretical limit set by the Cramer–Rao lower bound (CRLB). In order to improve the SNR and, consequently, to enhance the accuracy of the displacement estimation, a two-dimensional median filter may be applied to RF data [5]. In the case of an envelope-detected data, a linear Gaussian filter is used to improve the SNR in B-mode images [6].

Unlike [6], it is proposed here to use nonlinear filtering of the B-mode images for enhancing the accuracy of the displacement estimation in cardiac elastography. In this paper, the combined effect of a nonlinear filter and the kernel size on the accuracy of the displacement estimation is quantified and analyzed.

2. Two-dimensional tracking algorithm

Consider a sequence of B-mode images acquired from a human heart. For each frame j, $(j = 1, \ldots, J)$, a user-defined region of interest (ROI) is selected in image B_j. The pixel with maximal intensity is found in the ROI. This is assumed to be the position of the strongest reflector in the ROI. In order to estimate the position of this reflector in the next frame $j+1$, the 2D-tracking technique based on the computation of the normalized correlation coefficient is used [4]. As the first step of this technique, a "kernel" region is selected in image B_j—a rectangular region inside of the myocardium (Fig. 1). This kernel region from image B_j is correlated with identically sized regions (target regions) from a rectangular search area in image B_{j+1} acquired at the next frame. A rectangular search area in image B_{j+1} is centered at the position of a kernel region. At each spatial shift, the normalized correlation coefficient is computed between the kernel region from image B_j and the target region from image B_{j+1}, given by

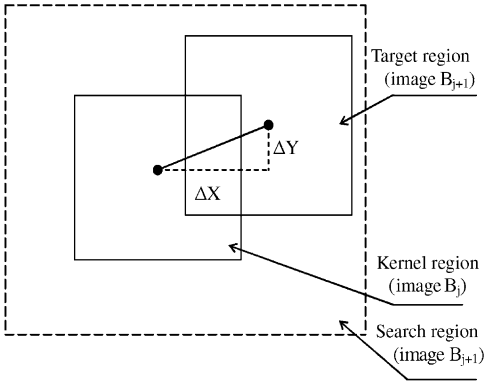

Fig. 1. Geometry for two-dimensional search.

$$\rho(k,l) = \frac{\sum_{m=1}^{M}\sum_{n=1}^{N}(b^{j}_{m,n} - \bar{b}^{j})(b^{j+1}_{m+k,n+l} - \bar{b}^{j+1})}{\sqrt{\sum_{m=1}^{M}\sum_{n=1}^{N}(b^{j}_{m,n} - \bar{b}^{j})^2 \sum_{m=1}^{M}\sum_{n=1}^{N}(b^{j+1}_{m+k,n+l} - \bar{b}^{j+1})^2}} \tag{1}$$

Here, $b^{j}_{m,n}$ represents the amplitude inside the kernel region at the pixel coordinates (m,n) and $b^{j+1}_{m+k,n+l}$ represents the amplitude inside the target region at the pixel coordinates $(m+k, n+l)$, k represents shift in the X-direction, l represents shift in the Y-direction, and $(M \times N)$ is the size of both the kernel and the target regions. The shifts of a target region, corresponding to the peak of the normalized cross-correlation coefficient $\rho(k,l)$, are assumed to be the displacement estimates.

3. The Cramer–Rao lower bound

The displacement estimate variance can be approximated from an analysis of the correlation errors, depending on the type of data used in a block-matching algorithm [7–11].

3.1. RF signal

When RF data is used, if the powers of the two signals being correlated are the same, and the measurement noise is additive and white, and is of a small magnitude with respect to the signal, the variance of the fluctuation of the peak position of the cross-correlation function (ξ) can be expressed by [7]:

$$(\sigma^2_{\xi})_{\text{axial}} = \frac{4\pi}{Q_{\text{axial}} \cdot \text{SNR}} \quad \text{and}$$
$$(\sigma^2_{\xi})_{\text{lateral}} = \frac{4\pi}{Q_{\text{lateral}} \cdot \text{SNR}} \tag{2}$$

where Q is the normalized second moment of the signal power spectrum. According to [7], this model is valid for fully correlated signals $(\rho = 1)$ and when the estimation window is very large. Assuming that the fractional bandwidth (BW) is defined as the width at half-maximum power of the Gaussian power spectrum, the value of Q in (2) can be found as [7]

$$Q_{\text{axial}} = \left(\frac{4\pi}{\lambda}\right)^2 \left(1 + \frac{\text{BW}^2}{8\ln 2}\right) \quad \text{and}$$
$$Q_{\text{lateral}} = 0.1\left(\frac{2\pi}{\lambda f_{\text{num}}}\right)^2 \tag{3}$$

where λ is the wavelength, $f_{\text{num}} = R/L$ is the F-number of an imaging system, R is the range, and L is the aperture length. Taking into account (3) and assuming that the SNR's are the same in both axial and lateral dimensions, the expressions for the displacement estimate variances are given by:

$$(\sigma_\xi^2)_{\text{axial}} = \frac{\lambda^2}{4\pi(1+\text{BW}^2/8\ln 2)\text{SNR}} \quad \text{and}$$
$$(\sigma_\xi^2)_{\text{lateral}} = 40(\sigma_\xi^2)_{\text{axial}} f_{\text{num}}^2 \left(1+\frac{\text{BW}^2}{8\ln 2}\right) \tag{4}$$

The smallest displacement errors (4) can be expressed using the CRLB. These errors can be achieved when operating under the small error condition (i.e. there is no ambiguity in the detection of the cross-correlation peak), and when the noise is white and Gaussian [8–11]. For the case of fully correlated signals ($\rho = 1$), the minimum variance of the axial displacement estimate (CRLB) is obtained for additive white Gaussian noise and relatively high SNR [8]:

$$(\sigma_\xi^2)_{\text{CRLB,axial}} = \frac{c^3}{8} \cdot \frac{1}{4\pi^2 f_0^3 \text{BW} \cdot W_{\text{axial}} \cdot \text{SNR}} \tag{5}$$

where c is the velocity of sound and W_{axial} is the length of an estimation window in range. For the case of partially correlated signals ($\rho \# 1$), the CRLB for the axial displacement estimate is obtained by Walker and Trahey in [9]:

$$(\sigma_\xi^2)_{\text{CRLB,axial}} = \frac{c^3}{8} \frac{3}{2\pi^2 f_0^3 \cdot W_{\text{axial}} \cdot (\text{BW}^3 + 12\text{BW})} \times \left[\frac{1}{\rho^2}\left(1+\frac{1}{\text{SNR}^2}\right)^2 - 1\right] \tag{6}$$

This expression predicts the jitter errors that occur when aligning broadband signals with flat power spectra, which have been corrupted by electronic noise and decorrelated by physical processes such as strain [10]. The SNR term in (2), (4), (5) and (6) represents only the contribution due to electronic noise. The predicted jitter magnitude is the minimum error achievable by any unbiased displacement estimation algorithm, including the cross-correlation.

3.2. Envelope signal

Varghese and Ophir have obtained the CRLB expression for axial displacement estimation for the case of envelope detected echo signals [10]. The expression is based on the results of Walker and Trahey, which were obtained for partially correlated RF signals [9]. The CRLB expression obtained by Varghese and Ophir is:

$$(\sigma_\xi^2)_{\text{CRLB,axial}} = \frac{c^3}{8} \frac{3}{2\pi^2 f_0^3 \cdot W_{\text{axial}} \cdot \text{BW}^3} \times \left[\frac{1}{\rho^2}\left(1+\frac{1}{\text{SNR}^2}\right)^2 - 1\right] \tag{7}$$

This expression predicts the lower bound of the jitter errors that occur while estimating the axial displacement between two partially correlated envelope signals, corrupted by electronic noise. The SNR term represents only the contribution due to electronic noise ($\text{SNR} = \text{SNR}_\text{E}$). In cardiac elastography, the correlation coefficient ρ in (7) varies with the applied strain and is itself dependent on the window length W_{axial}, used to compute the normalized cross-correlation function. In elastography, even if electronic noise is absent, undesired differences between signals kernel and target, influence the displacement estimation techniques. The main source of errors is the distortion of the signals due to tissue strain. Therefore, the correlation coefficient ρ in (7) can be rewritten in the form:

$$\rho = \rho_\text{E} \cdot \rho_\text{S} \tag{8}$$

where ρ_E represents decorrelation due to electronic noise and ρ_S represents decorrelation due to tissue strain. According to [10,11], the correlation coefficient can be converted into a SNR measure:

$$\rho_\text{E} = \frac{\text{SNR}_\text{E}}{1+\text{SNR}_\text{E}} \quad \text{and} \quad \rho_\text{S} = \frac{\text{SNR}_\text{S}}{1+\text{SNR}_\text{S}} \tag{9}$$

where SNR_E represents the contribution due to the signal decorrelation caused by electronic noise and SNR_S represents the contribution due to the signal decorrelation caused by strain. Taking into account (4)–(6) and (7), it may be concluded that in order to obtain good displacement estimates, high SNR due to electronic noise and a large estimation window (W_{axial}) are desirable. Furthermore, high SNR leads to high correlation coefficient ρ_E in (8) that reduces the estimation errors. The improvement in the SNR related to electronic noise (SNR_E) can be obtained by two-dimensional image filtration before cross-correlation. Although theoretical results about the CRLB for lateral displacement estimation have not been reported, the experimental results obtained by Ramamurthy and Trahey for two-dimensional motion estimation demonstrate the possibility to improve the accuracy of lateral displacement estimation by increasing the electronic SNR and the size of the estimation window [12].

4. Nonlinear filter description

In cardiac elastography, nonlinear filtering can be used to increase the electronic SNR in B-mode images, and thus improve the displacement estimation of moving elements within the cardiac muscle. Unlike linear filtering, nonlinear filtering may increase the SNR of the images while preserving important image elements. This study attempts to achieve this aim by testing three variants of nonlinear edge preserving filters, which are indicated in the literature as the most effective ones for this purpose. They are: (i) nonlinear Gaussian filter (or filter chain) that combines the aspects of anisotropic and robust filtering [13]; (ii) adaptive nonlinear anisotropic

diffusion filter that not only preserves edges but also enhances edges by inhibiting diffusion across edges and allowing diffusion on either side of the edge [14]; (iii) conventional linear unsharp filter that enhances edges while controlling sharpening [15].

4.1. Nonlinear Gaussian filters chain

According to [13], the algorithm of a nonlinear Gaussian filter is suggested to be:

$$G(\sigma_X,\sigma_Z,p)=f(p)+\frac{1}{N_p}\sum_{q\in P}g_X(\|p-q\|)\cdot g_Z(f(q)-f(p))\cdot(f(p)-f(q)) \tag{10}$$

with

$$g_X(t)=\exp\left(\frac{-t^2}{2\sigma_X^2}\right);\quad g_Z(t)=\exp\left(\frac{-t^2}{2\sigma_Z^2}\right);$$
$$N_p=\sum_{q\in P}g_X(\|q-p\|)g_Z(f(q)-f(p))$$

The weight function $g_X(t)$ is responsible for image smoothing while the function $g_Z(t)$ preserves the edges of the image. In order to enhance the noise reduction, a parameter can be added to the nonlinear Gaussian filter [13]:

$$G(\sigma_X,\sigma_Z,p)=f(p)+\frac{\eta}{N_p}\sum_{q\in P}g_X(\|p-q\|)\cdot g_Z(f(q)-f(p))\cdot(f(p)-f(q)) \tag{11}$$

According to [13], the parameter η should be in the range [1, 1.5]. In general, the smoothing effect of a single nonlinear Gaussian filter (10) may be not satisfactory. Therefore, several filters in series, with different parameters, σ_X and σ_Z, can be used. The first filter of the series serves mainly for reducing the contrast of the fine details of the images. The next stages continue this reduction, but at the same time sharpen the edges of the coarser structures, which have been blurred by the first step. Formally, the filter chain may be written as:

$$I_N=G_N(\sigma_{X,N},\sigma_{Z,N})G_{N-1}(\sigma_{X,N-1},\sigma_{Z,N-1})\ldots G_1(\sigma_{X,1},\sigma_{Z,1})I_0 \tag{12}$$

with $\sigma_{X,n}=2\sigma_{X,n-1}$ and $\sigma_{Z,n}=\sigma_{Z,n-1}/2$.

4.2. Adaptive anisotropic diffusion filter

An adaptive nonlinear anisotropic diffusion (AAD) technique must be used for improving the SNR of the ultrasound images. The theoretical and quantitative results obtained by Yu in [14] show that the AAD-filter could eliminate speckle and increase SNR without distorting useful image information and without destroying the important edges in the image. Formally, the iteration scheme of the AAD filter can be written in the form [14]:

$$I_{i,j}^{n+1}=I_{i,j}^n+\Delta t\cdot d_{i,j}^n/4 \tag{13}$$

where $I_{i,j}^n$ is the discretely sampled image, Δt is the time step size and $d_{i,j}^n$ are the divergence coefficients, which are calculated as:

$$d_{i,j}^n=c_{i+1,j}^n(I_{i+1,j}^n-I_{i,j}^n)+c_{i,j}^n(I_{i-1,j}^n-I_{i,j}^n)+c_{i,j+1}^n(I_{i,j+1}^n-I_{i,j}^n)+c_{i,j}^n(I_{i,j-1}^n-I_{i,j}^n) \tag{14}$$

with symmetric boundary conditions

$$d_{-1,j}^n=d_{0,j}^n;\quad d_{M,j}^n=d_{M-1,j}^n;\quad j=0,1,1,\ldots,N-1$$

$$d_{i,-1}^n=d_{i,0}^n;\quad d_{i,N}^n=d_{i,N-1}^n;\quad i=0,1,2,\ldots,M-1$$

The diffusion coefficients $c_{i,j}^n$ are given by:

$$c_{i,j}^n=c\left[q\left(\frac{1}{I_{i,j}^n}\sqrt{|\nabla_R I_{i,j}^n|^2+|\nabla_L I_{i,j}^n|^2},\frac{1}{I_{i,j}^n}\nabla^2 I_{i,j}^n\right)\right] \tag{15}$$

where

$$\nabla_R I_{i,j}^n=[(I_{i+1,j}^n-I_{i,j}^n),(I_{i,j+1}^n-I_{i,j}^n)];$$
$$\nabla_L I_{i,j}^n=[(I_{i,j}^n-I_{i-1,j}^n),(I_{i,j}^n-I_{i,j-1}^n)] \tag{16}$$

$$\nabla^2 I_{i,j}^n=I_{i+1,j}^n+I_{i-1,j}^n+I_{i,j+1}^n+I_{i,j-1}^n-4I_{i,j}^n \tag{17}$$

with symmetric conditions

$$I_{-1,j}^n=I_{0,j}^n;\quad I_{M,j}^n=I_{M-1,j}^n;\quad j=0,1,1,\ldots,N-1$$

$$I_{i,-1}^n=I_{i,0}^n;\quad I_{i,N}^n=I_{i,N-1}^n;\quad i=0,1,2,\ldots,M-1$$

The diffusion coefficients $c_{i,j}^n$ (15) are obtained as a result of discretization of the diffusion function $c(q)$, which can be chosen as:

$$c(q)=\frac{1}{1+[q^2(x,y,t)-q_0^2(t)]/[q_0^2(t)(1+q_0^2(t))]}\quad\text{or}$$
$$c(q)=\exp\left\{-\frac{q^2(x,y,t)-q_0^2(t)}{q_0^2(t)(1+q_0^2(t))}\right\} \tag{18}$$

where $q_0(t)$ is the speckle function, and $q(x,y,t)$ is the instantaneous coefficient of variation determined by

$$q(x,y,t)=\sqrt{\frac{(1/2)(|\nabla I|/I)^2-(1/4^2)(\nabla^2 I/I)^2}{[1+(1/4)(\nabla^2 I/I)]^2}} \tag{19}$$

where $I(x,y)$ is the image intensity. According to [14], the speckle function $q_0(t)$ can be approximated by

$$q_0(t)\approx q_0\exp(-\rho t) \tag{20}$$

where ρ is the constant and q_0 is the speckle coefficient of variation in the observed image. For fully developed speckle, $q_0=1$. The experimental results obtained in [14] show that the constant ρ could be chosen as 1/6.

4.3. Unsharp masking filter

The linear unsharp masking filter is also considered here, in order to compare the capabilities of linear and

nonlinear filters in improving the accuracy of the displacement estimation. According to [15], the unsharp masking filter subtracts from an image its Laplacian-of-Gaussian filtered version:

$$U(\sigma,k,I) = I - k \cdot \mathrm{LoG}(I,\sigma) \tag{21}$$

where $U(\sigma,k,I)$ is the output image, $\mathrm{LoG}(\sigma,I)$ is the Laplacian-of-Gaussian filtered version of the input image I, σ is the parameter of the Laplacian-of-Gaussian filter, and k is the parameter that controls the amount of sharpening. However, noise is also slightly amplified.

5. Numerical results

A sequence of grayscale B-mode images of a human heart is acquired using a VIVID III (GE Ultrasound Ltd, Tirat Hacarmel, Israel) ultrasound system operating at 1.77 MHz. The converted images are transferred to the file of movies for further off-line processing. The frame rate of the acquired images is 38 frames per second. One full cardiac cycle, including 36 frames, is used here for analysis of the accuracy of the displacement estimation. Four two-dimensional image ROIs (Fig. 2) are selected and used to investigate how the intensity of tracked reflectors influences the accuracy of the displacement estimation. The maximal intensity of the pixels inside the image regions ROI-1 and ROI-4, estimated at each frame, is very high (ROI with strong reflectors). It is distributed in the interval [220, 255]. On the other hand, the maximal intensity of the pixels inside the image regions ROI-2 and ROI-3, estimated at each frame, is quite low (ROI with weak reflectors). It is distributed in the interval [88, 163]. At the current frame i, $i = 1,\ldots,35$, the position of the pixel with maximal intensity is selected inside each ROI (ROI-1, ROI-2, ROI-3, ROI-4). The position of the kernel is defined as the position of this pixel. The new position of the kernel at the next frame $i+1$ is defined as the position of the peak of the cross-correlation function, between the kernel window of the image acquired at the current frame (i) and the target window of the image acquired at the next frame $(i+1)$ (Fig. 1). In our case, the processing of the experimental data by the cross-correlation technique shows that the maximal frame-to-frame displacement of a reflector inside the all selected ROI does not exceed six pixels in both dimensions (about 2.25 mm).

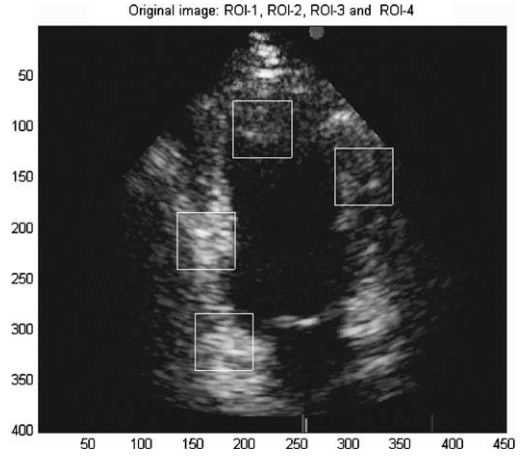

Fig. 2. ROI-2, ROI-3 (top) and ROI-1, ROI-4 (bottom).

There are two kinds of errors that occur in the displacement estimation when the two-dimensional correlation search algorithm is used [12]. These errors are classified according to the magnitude of the error between the correct and the estimated position of the correlation peak. The errors that occur when the estimated cross-correlation peak is within the central lobe of the correct cross-correlation curve (within the resolution cell) are called jitters. The errors that occur when the estimated cross-correlation peak is outside of this range are called false peaks. Such errors occur when the cross-correlation search algorithm finds falsely matched patterns. The accuracy of the displacement estimation can be expressed in terms of the root-mean square error (E_x, E_y) and the total number of false peaks (F). The root-mean-square errors are defined as:

$$E_X = \sqrt{\sum_{i=1}^{N_j} (x_i - x_{\mathrm{ref},i})^2 / N_j};$$

$$E_Y = \sqrt{\sum_{i=1}^{N_j} (y_i - y_{\mathrm{ref},i})^2 / N_j}, \quad N_j = N_{\mathrm{FRAME}} - F \tag{22}$$

where (x_i, y_i) is the displacement estimate at the current frame, $(x_{\mathrm{ref},i}, y_{\mathrm{ref},i})$ is its reference ("true") value, N_j is the total number of jitters, and N_{FRAME} is the number of frames. The total number of false peaks (F) is defined as:

$$F = \sum_{i=1}^{35} f_{X,i} \cdot f_{Y,i};$$

$$f_{X,i} = \begin{cases} 1, & \text{if } |x_i - x_{\mathrm{ref},i}| > \delta_X/2 \\ 0, & \text{otherwise} \end{cases};$$

$$f_{Y,i} = \begin{cases} 1, & \text{if } |y_i - y_{\mathrm{ref},i}| > \delta_Y/2 \\ 0, & \text{otherwise} \end{cases} \tag{23}$$

where (δ_X, δ_Y) is the size of the spatial resolution cell of the system in the X- and Y-directions, respectively. The reference value $(x_{\mathrm{ref},i}, y_{\mathrm{ref},i})$ can be defined as an estimate obtained when using a window that guarantees maximal estimation accuracy. The required size of a reference window may be based on the experimental results obtained by Ramamurthy and Trahey in [12]. According to their results, in the case of envelope-detected data, the cross-correlation algorithm performs with 97% accuracy for target translation of up to 2.25 mm, if the window

size is greater than nine spatial resolution cells. Here, the spatial resolution cell (δ_X, δ_Y) is estimated experimentally using the 36-frame sequence of the B-mode images. The size of the spatial resolution cell in the X- and Y-dimensions can be found as the full width at half the maximum (FWHM) of the corresponding autocorrelation function of the system. At each frame, the FWHM-estimate is computed for the strongest reflector inside the selected ROI. The maximal size of the spatial resolution cell found in the present net of experimental data is (17×23) pixels for ROI-1, (9×19)—for ROI-2, (13×11)—for ROI-3 and (13×29)—for ROI-4. According to the graphical results of Ramamurthy and Trahey in [12], it could be expected that a window of size (75×75), which includes about 15 spatial resolution cells of size (17×23), can be used as a window for estimating the reference value $(x_{\mathrm{ref},i}, y_{\mathrm{ref},i})$. This can be expected because the maximal frame-to-frame displacement of a reflector inside each of the selected ROI does not exceed six pixels or 2.25 mm.

5.1. Impact of the window size

In order to study the impact of the window size on the accuracy of the displacement estimation, both estimation errors, the root-mean square errors (E_X, E_Y) and the number of false peaks (F), are computed for nine variants of windows $Wk = K \cdot \delta_X \cdot \delta_Y$ $(K = 1; 1.5; 2; 2.5; 3; 3, 5; 4; 5; 6)$ as shown in Table 1. The kernel window for each ROI varies in range from one resolution sell $(\delta_X \times \delta_Y)$ to six resolution cells $(6 \times \delta_X \times \delta_Y)$. Taking into account the CRLB expression for axial displacement estimation (7), it is theoretically expected, that the accuracy will improve with increased window size, due to the increase in information content within the kernel and the target regions. Indeed, the numerical results presented in Tables 2–5 for the original image show that for each selected ROI, the root-mean-square errors E_X and E_Y are reduced twofold when the window increases from one resolution cell to six resolution cells. The error in the X-direction is greater than the error in the Y-direction for regions ROI-1, ROI-2, ROI-4 and less so for ROI-3. Obviously, the E_X-to-E_Y ratio varies when varying the angle of view. As shown in Tables 2–5, the number of false peaks F drastically reduces when with the window size is increased. The number of false peaks reduces from 8 to 0—for ROI-4, from 10 to 0—for ROI-2 and from 6 to 1—for ROI-3, when the window is increased from one resolution cell to six resolution cells. It must be emphasized that very large kernel sizes translate into broadening of the main lobe of the autocorrelation function, which causes a loss in the spatial resolution of the motion estimation and the strain imaging. Therefore, the kernel size should be chosen very carefully, as the result of a compromise between the desired accuracy of the displacement estimation and the desired resolution of the strain images. The optimal window size must be the minimal size that guarantees the required accuracy of estimation.

It may be concluded that windows of size $W = 2.5 \cdot (\delta_X \times \delta_Y)$—for ROI-1, $W = 5 \cdot (\delta_X \times \delta_Y)$—for ROI-2, $W = 3 \cdot (\delta_X \times \delta_Y)$—for ROI-3, and $W = 6 \cdot (\delta_X \times \delta_Y)$—for ROI-4 guarantee root-mean-square errors of less than one pixel $(E_X < 1, E_Y < 1)$ under the minimum number of false peaks $(F = 0–1)$.

Table 1
Different window sizes defined in terms of the resolution volume of the system

Number of resolution volumes (K)	Window size $Wk = K\cdot$ resolution volume			
	ROI-1	ROI-2	ROI-3	ROI-4
1	17×23	9×19	13×11	13×29
1.5	21×29	11×23	15×13	15×35
2	23×33	13×27	19×15	19×41
2.5	27×37	15×29	21×17	21×45
3	29×39	15×33	23×19	23×51
3.5	31×43	17×35	25×21	25×55
4	33×45	17×37	27×23	27×57
5	37×51	21×43	29×25	29×65
6	41×55	23×47	31×27	31×71

Table 2
Root-mean-square errors (E_x and E_y), and number of false estimates (*False peaks*) computed for ROI-1

Window (K)	Original image			AAD-filter			Nonlinear Gaussian filter chain			Unsharp masking filter		
	E_X (pxl)	E_Y (pxl)	False peaks	E_X (pxl)	E_Y (pxl)	False peaks	E_X (pxl)	E_Y (pxl)	False peaks	E_X (pxl)	E_Y (pxl)	False peaks
1	1.34	0.5	0	0.96	0.56	1	0.94	0.53	1	1.5	0.37	1
1.5	1.03	0.49	0	0.77	0.61	0	0.78	0.6	0	1.38	0.39	0
2	1.04	0.46	0	0.73	0.6	0	0.74	0.57	0	1.3	0.35	0
2.5	0.98	0.46	0	0.65	0.49	0	0.66	0.5	0	0.94	0.31	0
3	0.96	0.33	0	0.63	0.47	0	0.61	0.47	0	0.87	0.28	0
3.5	0.95	0.27	0	0.52	0.4	0	0.56	0.37	0	0.95	0.24	0
4	0.92	0.24	0	0.51	0.36	0	0.54	0.36	0	0.93	0.23	0
5	0.76	0.22	0	0.42	0.32	0	0.43	0.33	0	0.78	0.21	0
6	0.53	0.2	0	0.34	0.3	0	0.38	0.29	0	0.57	0.26	0

Table 3
Root-mean-square errors (E_x and E_y), and number of false estimates (*False peaks*) computed for ROI-4

Window (K)	Original image			AAD-filter			Nonlinear Gaussian filter chain			Unsharp masking filter		
	E_X (pxl)	E_Y (pxl)	False peaks	E_X (pxl)	E_Y (pxl)	False peaks	E_X (pxl)	E_Y (pxl)	False peaks	E_X (pxl)	E_Y (pxl)	False peaks
1	2.8	1.17	8	2.99	1.34	4	2.32	1.34	6	4.05	1.81	6
1.5	2.52	1.25	7	2.85	1.23	4	2.85	1.24	4	4.3	1.76	6
2	3.34	1.05	2	1.65	1.08	3	1.72	1.13	3	3.86	1.14	3
2.5	3.25	1.4	2	1.92	0.95	2	2.06	0.98	2	3.25	1.27	1
3	3.21	1.43	1	2.88	0.88	0	2.9	0.86	0	2.95	1.11	1
3.5	2.46	0.95	0	1.6	0.82	0	1.7	0.84	0	2.66	0.94	0
4	1.79	0.94	0	1.43	0.81	0	1.5	0.80	0	2.49	0.93	0
5	1.22	0.93	0	1.1	0.74	0	1.12	0.73	0	1.49	0.92	0
6	0.93	0.83	0	0.9	0.69	0	0.94	0.70	0	1.00	0.98	0

Table 4
Root-mean-square errors (E_x and E_y), and number of false estimates (*False peaks*) computed ROI-2

Window (K)	Original image			AAD-filter			Nonlinear Gaussian filter chain			Unsharp masking filter		
	E_X (pxl)	E_Y (pxl)	False peaks	E_X (pxl)	E_Y (pxl)	False peaks	E_X (pxl)	E_Y (pxl)	False peaks	E_X (pxl)	E_Y (pxl)	False peaks
1	1.66	0.51	10	1.4	0.83	8	1.35	0.52	10	2.44	0.57	11
1.5	1.76	0.47	5	1.4	0.63	4	1.4	0.61	5	1.64	0.52	6
2	1.6	0.46	5	1.48	0.6	2	1.5	0.62	3	1.65	0.42	5
2.5	1.53	0.4	4	1.4	0.54	1	1.38	0.56	1	1.06	0.49	3
3	0.72	0.4	2	1.14	0.5	1	1.11	0.53	1	0.98	0.46	3
3.5	0.73	0.4	1	1.0	0.48	1	1.72	0.51	0	0.89	0.47	2
4	0.72	0.4	1	0.95	0.47	1	1.63	0.48	0	0.86	0.47	2
5	0.85	0.39	0	0.73	0.45	1	1.28	0.46	0	1.0	0.44	0
6	0.71	0.37	0	0.71	0.41	1	0.72	0.45	0	0.87	0.39	0

Table 5
Root-mean-square errors (E_x and E_y), and number of false estimates (*False peaks*) computed for the region of interest ROI-3

Window (K)	Original image			AAD-filter			Nonlinear Gaussian filter chain			Unsharp masking filter		
	E_X (pxl)	E_Y (pxl)	False peaks	E_X (pxl)	E_Y (pxl)	False peaks	E_X (pxl)	E_Y (pxl)	False peaks	E_X (pxl)	E_Y (pxl)	False peaks
1	0.84	0.71	6	1.18	1.3	9	1.26	0.8	10	1.12	0.53	7
1.5	0.82	0.64	3	1.0	1.29	5	1.01	1.3	5	1.08	0.49	5
2	0.94	0.7	3	1.0	1.15	4	1.0	1.17	4	0.98	0.49	7
2.5	0.84	0.67	2	0.88	1.15	4	0.85	1.14	4	0.81	0.53	5
3	0.74	0.84	1	0.76	1.16	2	0.78	1.16	2	0.84	0.51	3
3.5	0.71	0.86	1	0.66	0.76	3	0.68	0.72	3	0.83	0.5	3
4	0.61	0.84	1	0.57	0.75	2	0.58	0.7	2	0.81	0.5	3
5	0.59	0.82	1	0.46	0.65	2	0.48	0.65	2	0.8	0.48	3
6	0.57	0.82	1	0.49	0.65	1	0.43	0.62	2	0.79	0.5	3

5.2. Impact of nonlinear filtering

In order to study how the preprocessing by the nonlinear filtering influences the accuracy of the displacement estimation, the experimental 35-frame sequence of B-mode images was filtered before applying the cross-correlation algorithm. Both estimation errors, (E_X, E_Y) and F, are computed for three filters: (i)—adaptive anisotropic diffusion, (ii)—nonlinear Gaussian filter chain with three iterations, (iii)—unsharp masking filter. The numerical results are summarized in Tables 2–5 and plotted in Figs. 3–14.

In image regions with strong reflectors, such as ROI-1 and ROI-4, the preprocessing of the images by the nonlinear Gaussian filter chain and by the adaptive anisotropic diffusion filter can improve the accuracy of the displacement estimation. As shown in Table 2, for the image region ROI-1, the root-mean-square error was less than one pixel and the number of false peaks was zero for a window $W = 2.5 \cdot (\delta_X \times \delta_Y)$ without filtering.

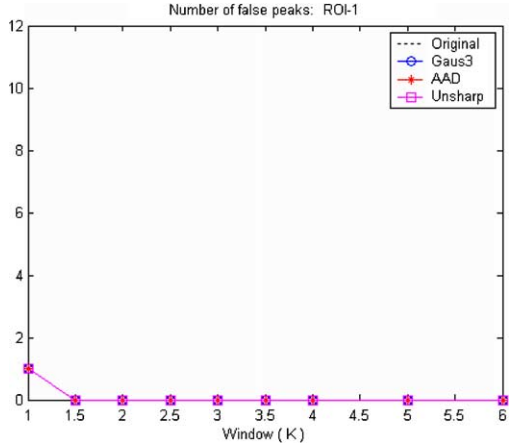

Fig. 3. Number of false peaks estimated in ROI-1 for different types of images and windows.

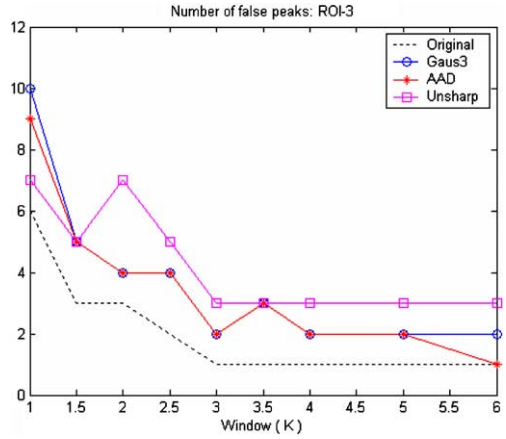

Fig. 6. Number false peaks estimated in ROI-3 for different types of images and windows.

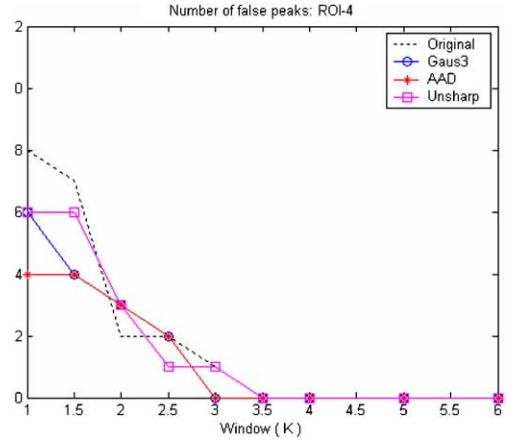

Fig. 4. Number false peaks estimated in ROI-4 for different types of images and windows.

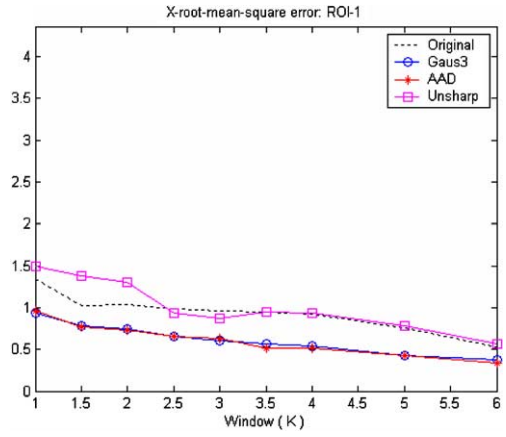

Fig. 7. Root-mean square error in X-direction for different types of images and windows (ROI-1).

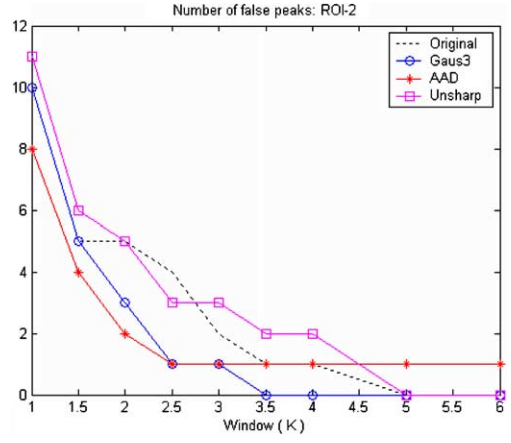

Fig. 5. Number of false peaks estimated in ROI-2 for different types of images and windows.

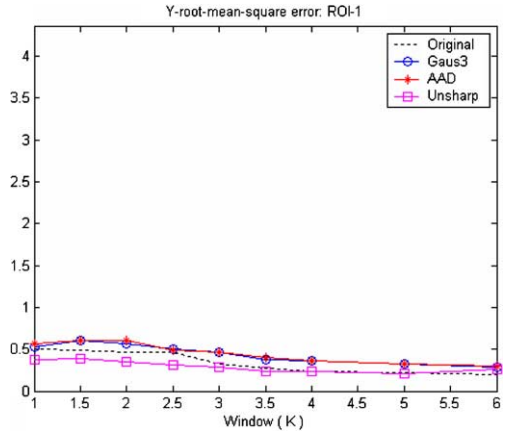

Fig. 8. Root-mean square error in Y-direction for different types of images and windows (ROI-1).

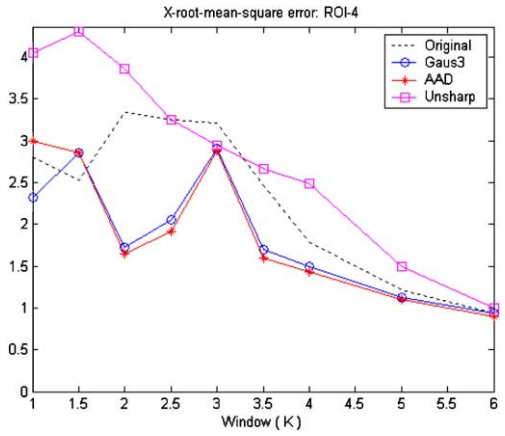

Fig. 9. Root-mean square error in X-direction for different types of images and windows (ROI-4).

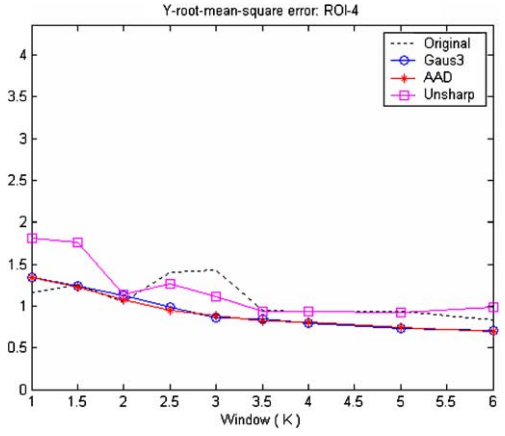

Fig. 10. Root-mean square error in Y-direction for different types of images and windows (ROI-4).

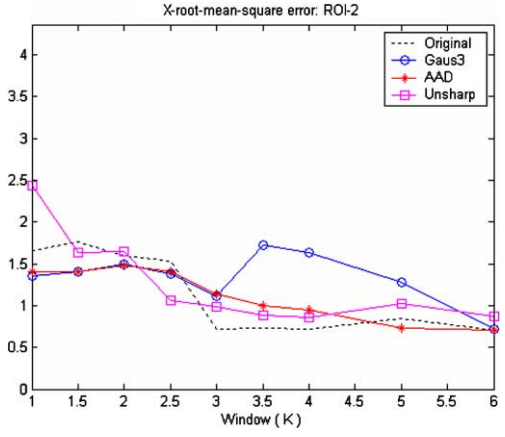

Fig. 11. Root-mean square error in X-direction for different types of images and windows (ROI-2).

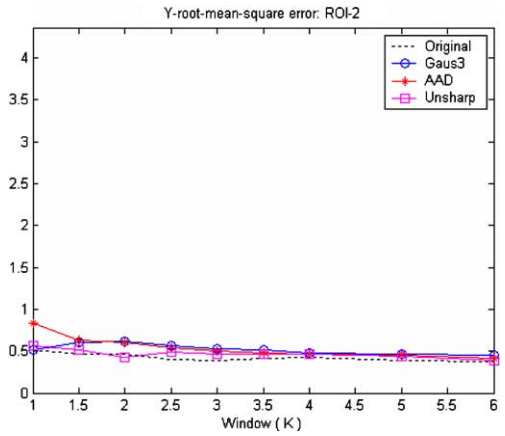

Fig. 12. Root-mean square error in Y-direction for different types of images and windows (ROI-2).

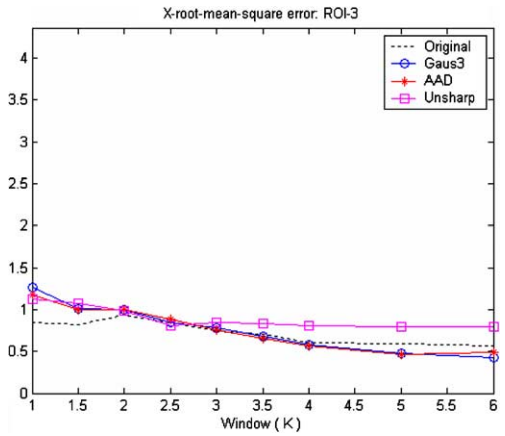

Fig. 13. Root-mean square error in X-direction for different types of images and windows (ROI-3).

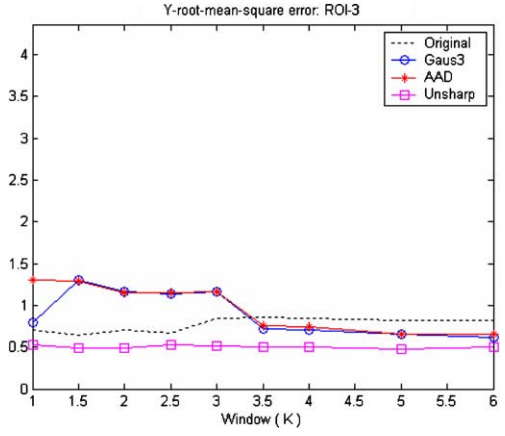

Fig. 14. Root-mean square error in Y-direction for different types of images and windows (ROI-3).

However, better accuracy can be obtained with a smaller window, $W = 1.5 \cdot (\delta_X \times \delta_Y)$, if a Gaussian filter chain or an anisotropic diffusion filter are first used for image filtration. Indeed, on the one hand the very large window improves the accuracy of estimation. On the other hand the very large window broadens the main lobe of

the autocorrelation function causing a loss in the spatial resolution of the motion estimation and the strain imaging. Therefore, the optimal window should be chosen as a minimal window that guarantees the required accuracy of displacement estimation. That is why the window $W = 1.5 \cdot (\delta_X \times \delta_Y)$ is the optimal window because guarantees the root-mean-square error less than one pixel without false peaks The linear filtration with an unsharp masking filter does not improve the accuracy of the estimation in this region. The numerical results in Table 3 show, that in the image region ROI-4, root-mean-square error of less than two pixels and zero false peaks are obtained for a window $W = 4 \cdot (\delta_X \times \delta_Y)$ without filtering. Better accuracy can be achieved with a smaller window size, $W = 3.5 \cdot (\delta_X \times \delta_Y)$ if the nonlinear filtering is used before the calculation of the cross-correlation. The window $W = 6 \cdot (\delta_X \times \delta_Y)$ guarantees that the root-mean-square errors are of less than one pixels and the number of false peaks is zero without filtering. The same window, however, allows reduction of the errors E_X and E_Y from 0.93 pixels to 0.9 and from 0.83 to 0.69, respectively, if nonlinear filtering is first used.

In image regions with relatively weak reflectors, such as ROI-2 and ROI-3, the influence of nonlinear filtration on the accuracy of the displacement estimation is very weak. As shown in Table 4, nonlinear filtering reduces the number of false peaks if the window size is relatively small ($K < 4$). When the window size is large enough ($K = 5, 6$) and the number of false peaks is small, the nonlinear filtration does not improve the accuracy of the estimation. The root-mean-square errors in the X- and Y-directions are about 0.7 and 0.4 for both cases (with filtering and without filtering) when the window of size $W = 6 \cdot (\delta_X \times \delta_Y)$ is used for the estimation. The same conclusion is drawn from the analysis of the results obtained for the image region ROI-3 (Table 5). When the window size is large enough ($K > 3.5$) the root-mean-square errors in both directions are slightly improved with nonlinear filtering. If the window of size $W = 6 \cdot (\delta_X \times \delta_Y)$ is used for the cross-correlation estimation, the error in the X-direction is reduced from 0.57 to 0.49 pixels—for an anisotropic diffusion filter, and to 0.43 pixels—for a Gaussian filter chain. The error in the Y-direction is reduced from 0.82 to 0.65 pixels—for an anisotropic diffusion filter, and to 0.62 pixels—for a Gaussian filter chain.

6. Conclusion

It is shown that the performance of two-dimensional displacement estimation can be improved by preprocessing nonlinear filtration of the B-mode images only for the case of very strong reflectors. Under these conditions the required accuracy of the displacement estimation can be achieved while using smaller sizes of the estimation windows than without filtering. The smaller size of the estimation window leads to smaller losses of spatial resolution of the motion estimation. In elastography, that translates into improvements in resolution of the strain images. The numerical results show that an adaptive anisotropic diffusion filter or a nonlinear Gaussian filter chain can be effectively used for improving the quality of elastograms in image regions with strong reflectors. The linear filtration with an unsharp masking filter does not improve the accuracy of the estimation in these regions.

In image regions with relatively weak reflectors, the influence of nonlinear filtration on the accuracy of the displacement estimation is not significant and the improvement of the estimation accuracy is relatively small.

Acknowledgements

The authors are grateful to the Technion-Israel Institute of Technology, VPR—the promotion of Research Fund, to the IZMEL consortium, supported by the Ministry of Industry and Commerce, and to the Center for Absorption in Science, Ministry of Immigrant Absorption, Israel, for the financial support of this work.

References

[1] J. Ophir, E. Géspedes, H. Ponnenkanti, Y. Yazdi, X. Li, Elastography: a quantitative method for imaging the elasticity of biological tissues, Ultrason. Imag. 13 (1991) 111–134.
[2] J. D'hooge, A. Heimdal, F. Jamal, T. Kukulski, B. Bijnens, F. Rademakers, L. Hatle, P. Suetens, G. Sutherland, Regional strain and strain rate measurements by cardiac ultrasound: principles, implementations and limitations, Eur. J. Echocardiogr. 1 (2000) 154–170.
[3] E. Konofagou, T. Harrigan, S. Solomon, Assessment of regional myocardial strain using cardiac elastography: distinguishing infracted from non-infarcted myocardium, IEEE Ultrasonic Symposium, 2001, pp. 1589–1592.
[4] G. Trahey, S. Hubbard, O. von Ramm, Angle independent ultrasound blood flow detection by frame-to-frame correlation of B-mode images, IEEE Ultrasonic Symposium, 1988, pp. 271–276.
[5] L. Bohs, G. Trahey, A novel method for angle independent ultrasonic imaging of blood flow and tissue motion, IEEE Trans. Ultras. Ferro. Freq. Contr. 38 (1991) 280–286.
[6] F. Yeung, S. Levinson, K. Parker, Multilevel and motion model-based ultrasonic speckle tracking algorithms, Ultras. Med. Biol. 24 (1998) 427–441.
[7] M. Lubinski, S. Emelianov, K. Raghavan, A. Yagle, A. Skovoroda, M. O'Donnell, Lateral displacement estimation using tissue incompressibility, IEEE Trans. Ultras. Ferro. Freq. Contr. 43 (1996) 247–256.
[8] E. Géspedes, M. Insana, J. Ophir, Theoretical bounds on strain estimation in elastography, IEEE Trans. Ultras. Ferro. Freq. Contr. 42 (1995) 969–972.
[9] W. Walker, G. Trahey, A fundamental limit on delay estimation using partially correlated speckle signals, IEEE Trans. Ultras. Ferro. Freq. Contr. 42 (1995) 301–308.
[10] T. Varghese, J. Ophir, A theoretical framework for performance characterization of elastography: The strain filter, IEEE Trans. Ultras. Ferro. Freq. Contr. 44 (1997) 164–172.

[11] T. Varghese, J. Ophir, Characterization of elastography noise using the envelope of echo signals, Ultras. Med. Biol. 24 (1998) 543–555.
[12] B. Ramamurthy, G. Trahey, Potential and limitations of angle-independent flow detection algorithms using radio frequency and detected echo signals, Ultras. Imag. 13 (1991) 252–268.
[13] V. Aurich, J. Weule, Non-linear Gaussian filters performing edge preserving diffusion, 17th DAGM Symposium, Bielefeld, 1995, pp. 538–545.
[14] Y. Yu, Speckle reducing anisotropic diffusion, IEEE Trans. Imag. Proc. 11 (2002) 1260–1270.
[15] R. Schalkoff, Digital image processing and computer vision, John Wiley & Sons, 1989.